Exact-Two-Component Complete Active Space Method with Variational Treatment of Magnetic Field and Spin-Orbit Coupling: Application to X-ray Magnetic Circular Dichroism Spectroscopy

Diandong Tang,[†] Shichao Sun,[‡] and Xiaosong Li[*,†]

†*Department of Chemistry, University of Washington, Seattle, USA 98195*

‡*Department of Chemistry and Department of Physics & Astronomy, University of California, Irvine, USA 92697*

E-mail: xsli@uw.edu

Abstract

We introduce an exact-two-component complete active space self-consistent-field (X2C-CASSCF) method formulated under the restricted-magnetic-balance condition. This framework allows for the non-perturbative treatment of static magnetic fields using gauge-including atomic orbitals (GIAOs). The GIAO-X2C-CASSCF methodology effectively captures all microstates within the same $2J+1$-degenerate manifold and their splitting in a static magnetic field, which are not accessible through single-reference-based methods. We also present mathematical recursive expressions for evaluating one-electron relativistic integrals using GIAOs in the presence of a finite magnetic field. Benchmark studies include oxygen and nitrogen K-edge X-ray magnetic circular dichroism spectroscopy (XMCD) for closed-shell organic compounds, as well as L-edge XMCD spectroscopy for the high-spin open-shell transition metal ion Mn^{2+} and the tetrahedral $Mn(II)O_4^{6-}$ complex.

1 Introduction

Magnetic Circular Dichroism (MCD) spectroscopy is a sensitive probe that measures the difference in electron absorption between left and right circularly polarized (LCP/RCP) photons in the presence of a static magnetic field.[1–3] An external magnetic field can split the spin and/or angular momentum of an electron, causing degenerate energy levels to separate, a phenomenon known as the Zeeman effect. Left and right circularly polarized photons follow different selection rules for the total angular momentum quantum number, resulting in a differential spectrum that is also temperature-dependent when the ground state exhibits Zeeman splitting. Using high-energy x-ray photons in MCD (XMCD) offers additional element-specific fingerprints through core-electron excitations, such as the $L_{2,3}$ edges for $3d$ transition metals and the $M_{4,5}$ edges for late-row elements, which split due to the spin-orbit coupling.[4–6]

The MCD technique has been successfully employed in the characterization of magnetic defects in materials[7–15] and in the investigation of ultrafast magnetization dynamics.[12,16–19] Recent work has shown that time-resolved X-ray MCD is able to track wavepacket dynamics and directly identify the conical intersection in photochemical processes.[20] Although MCD spectroscopy has proven to be a powerful technique in these experiments that provides rich insights into the magnetic and spin properties of molecular and material systems, the theoretical treatment of MCD is a non-trivial task. This complexity arises from the need to simultaneously account for relativistic effects, magnetic field perturbations, and the response to circularly polarized probing light, as well as the intricate interplay between these factors.

Perturbative treatments of the magnetic field and spin-orbit interactions have been developed within the quadratic response function,[21] the complex polarization propagator method,[22–24] time-dependent density functional theory (TDDFT),[25–27] multi-configurational self-consistent field theory (MCSCF),[28–30] and the resolution-of-identity coupled cluster singles-and-approximate-doubles (RI-CC2),[31] and have seen great successes in modeling MCD.

Recent developments in variational approaches within the single reference framework

(*e.g.*, two-component time-dependent Hartree-Fock and two-component TDDFT) have significantly expanded the capabilities of computational MCD.[31–37] These advancements, formulated in the relativistic Dirac equation and utilizing integrals with finite-magnetic-field gauge-including atomic orbitals (GIAO), enable accurate simulations of MCD in strong magnetic field and strong spin-orbit regimes and facilitate the modeling of temperature dependence. Unlike response theory-based perturbative approaches, variational methods incorporate both spin-orbit and magnetic field effects at the molecular orbital level, requiring only the transition dipoles between states for MCD evaluation. It is crucial to emphasize that the accurate simulation of relativistic effects in strong magnetic fields requires the Dirac equation to be formulated under the magnetic balance condition.[35] This condition ensures a smooth transition from a fully relativistic to a non-relativistic treatment of electronic structure, providing accurate and consistent results across different regimes.

While single-reference-based variational approaches open a new avenue for simulating MCD, they are currently limited to closed-shell or open-shell systems with a single unpaired electron. However, transition metal complexes and magnetic defects often exhibit complex electronic structures and magnetic behaviors arising from multiple unpaired d and f electrons. Expanding the capabilities of variational approaches to handle these more complex systems will be a significant step forward in computational MCD.

In this work, we introduce a relativistic exact-two-component complete active space self-consistent-field approach (X2C-CASSCF)[38,39] formulated within the restricted magnetic-balance (RMB) condition and finite-magnetic-field GIAO. We showcase this new approach through modeling the X-ray MCD (XMCD) of molecular complexes, where the intricate interplays between core- and valence-electron spin-orbit couplings and magnetic fields are probed by circularly polarized x-ray photons.

2 Methodology

2.1 Temperature-Dependent MCD Strength

MCD is a universally applicable probe of molecular systems, as the introduction of a magnetic field breaks time-reversal symmetry. In contrast, natural circular dichroism is specific to certain chiral or helical molecules that break inversion symmetry. In the variational MCD method, the ground and excited state wavefunctions are optimized by incorporating the external magnetic field and relativistic effects into the Hamiltonian. Time-reversal symmetry breaking is manifested in the wavefunction and energy of the microstates. Defining direction of incident light and magnetic field as γ, the left and right circularly polarized (LCP and RCP) dipoles are defined from the point of view of the observer as:

$$\mu_\gamma^- = \frac{1}{2}(\mu_\alpha - i\mu_\beta) \tag{1}$$

$$\mu_\gamma^+ = \frac{1}{2}(\mu_\alpha + i\mu_\beta) \tag{2}$$

Consequently, the formula for computing the MCD strength can be readily expressed as follows:[1,35]

$$\frac{\Delta A}{\mathcal{E}} = \Gamma \sum_J \left(i \sum_{\alpha\beta\gamma} \epsilon_{\alpha\beta\gamma} \langle 0|\mu_\alpha|J\rangle^\gamma \langle J|\mu_\beta|0\rangle^\gamma \right) f(\hbar\omega - \hbar\omega_{0J}^\gamma), \tag{3}$$

where $\gamma \in \{x, y, z\}$ is the direction of the magnetic field ($\mathbf{B}$) and $\epsilon_{\alpha\beta\gamma}$ is the Levi-Civita symbol ($\epsilon_{xyz,yzx,zxy} = 1$, $\epsilon_{yzx,zyx,xzy} = -1$; otherwise 0). μ is the dipole operator. $\mathcal{E}$ is photon energy and Γ is a collection of physical constants. ω_{0J} is the excitation energy from the ground state $|0\rangle$ to the excited state $|J\rangle$.

In cases where the ground state consists of multiple degenerate microstates due to spin or spin-orbit multiplicity, *i.e.*, $S > 0$ and $J > 0$, the interaction between angular momentum

and the external magnetic field will split these microstates into non-degenerate levels. The thermal population of these microstates results in temperature-dependent MCD. The working equation for temperature-dependent MCD is a weighted average of state-specific MCDs, determined by the Boltzmann distribution:[1,35]

$$\frac{\Delta A}{\mathcal{E}} = \Gamma \sum_{k}^{N_0} \frac{N_k}{\sum_{k}^{N_0} N_k} \sum_{J} \left(i \sum_{\alpha\beta\gamma} \epsilon_{\alpha\beta\gamma} \langle 0_k | \mu_\alpha | J \rangle^\gamma \langle J | \mu_\beta | 0_k \rangle^\gamma \right) f(\hbar\omega - \hbar\omega_{0J}^\gamma), \tag{4}$$

where N_0 is number of near-degenerate microstates and $N_k = e^{-E_k/k_\mathrm{B}T}$ is the Boltzmann distribution of each microstate k.

2.2 CASSCF with Gauge-Including Atomic Orbitals and Relativistic Effects – GIAO-X2C-CASSCF

To describe the splitting of microstates due to the interaction between the magnetic field and spin-orbit coupling, three key components are integrated into a computational MCD approach: (1) the use of finite-magnetic-field GIAO to define a local gauge origin on each atom, thus mitigating the gauge origin dependence, (2) the X2C relativistic approach to variationally incorporate one-electron relativistic effects, including the scalar relativistic effects and spin-orbit effects, as well as the magnetic field-molecule interaction in the wavefunction optimization, and (3) a multireference method within the framework of CASSCF to effectively model near-degenerate microstates. This approach will be referred to as GIAO-X2C-CASSCF.

2.2.1 Finite-Magnetic-Field Gauge-Including Atomic Orbital

For many-atom systems, electronic structure calculations in the presence of electromagnetic fields can become unphysically dependent on the choice of the arbitrary gauge origin. By using GIAOs, also known as London orbitals,[40–49] a local gauge origin is defined on each nuclear center, removing the gauge origin dependence in the simulation. The expression for

GIAO is given by:

$$\chi^{\mathrm{GIAO}}(\mathbf{r}, \mathbf{k}_A) = \chi^{\mathrm{GTO}}(\mathbf{r} - \mathbf{R}_A) e^{i\mathbf{k}_A \cdot (\mathbf{r} - \mathbf{R}_A)}, \tag{5}$$

where magnetic field $\mathbf{B}$ and gauge center $\mathbf{R}_A$ (set as the center of the basis) enter the expression as a phase factor $\mathbf{k}_A = \frac{1}{2}(\mathbf{R}_A \times \mathbf{B})$ for the Gaussian-type orbitals (GTO). General recursion relationships for one- and two-electron integrals using London orbitals with a finite-magnetic-field have been previously developed.[50–53]

2.2.2 Exact-Two-Component in Restricted Magnetic-Balance Condition

The theory of the restricted-magnetic-balance (RMB) condition was introduced previously,[35,54–59] ensuring a smooth transition from relativistic to non-relativistic, and from magnetic-field-dressed to non-magnetic electronic structure calculations. The RMB condition allows the same basis to be used for the large and pseudo-large components in the bi-spinor representation, supporting the one-step exact-two-component (X2C) transformation from four-component to two-component framework.[60–79]

In the spinor basis, the matrix representation of the Dirac equation in RMB is:

$$\begin{pmatrix} \mathbf{V} & \mathbf{M} \\ \mathbf{M} & \frac{1}{4c^2}\mathbf{W} - \mathbf{M} \end{pmatrix} \begin{pmatrix} \mathbf{C}_L^+ & \mathbf{C}_L^- \\ \mathbf{C}_S^+ & \mathbf{C}_S^- \end{pmatrix} = \begin{pmatrix} \mathbf{S} & \mathbf{0} \\ \mathbf{0} & \frac{1}{2c^2}\mathbf{M} \end{pmatrix} \begin{pmatrix} \mathbf{C}_L^+ & \mathbf{C}_L^- \\ \mathbf{C}_S^+ & \mathbf{C}_S^- \end{pmatrix} \begin{pmatrix} \boldsymbol{\epsilon}^+ & \mathbf{0} \\ \mathbf{0} & \boldsymbol{\epsilon}^- \end{pmatrix} \tag{6}$$

$$M_{\mu\nu} = \langle f_\mu | \frac{1}{2} (\boldsymbol{\sigma} \cdot \boldsymbol{\pi})(\boldsymbol{\sigma} \cdot \boldsymbol{\pi}) | f_\nu \rangle \tag{7}$$

$$W_{\mu\nu} = \langle f_\mu | (\boldsymbol{\sigma} \cdot \boldsymbol{\pi}) V (\boldsymbol{\sigma} \cdot \boldsymbol{\pi}) | f_\nu \rangle \tag{8}$$

The mechanical momentum $\boldsymbol{\pi} = \mathbf{p} + \mathbf{A}$ includes the linear momentum $\mathbf{p} = i\boldsymbol{\nabla}$ and the vector potential $\mathbf{A} = \frac{1}{2}\mathbf{B} \times \mathbf{r}$ for electrons. Each spinor is formed as a tensor product of a GIAO $\tilde{\chi}$ with spin functions $f = \{\tilde{\chi}\} \otimes \{\alpha, \beta\}$. where $\mathbf{S}$ and $\mathbf{V}$ are the block-diagonal two-component overlap and non-relativistic potential energy matrix, and $\{\epsilon_p^+\}$, $\{\epsilon_p^-\}$ are

the sets of positive/negative eigenvalues with corresponding molecular orbital coefficients $(\mathbf{C}_L^+ \quad \mathbf{C}_S^+)^T$ for the positive and $(\mathbf{C}_L^- \quad \mathbf{C}_S^-)^T$ for the negative energy solutions. $M_{\mu\nu}$ and $W_{\mu\nu}$ are matrix elements of operator $\frac{1}{2}(\boldsymbol{\sigma}\cdot\boldsymbol{\pi})(\boldsymbol{\sigma}\cdot\boldsymbol{\pi})$ and $(\boldsymbol{\sigma}\cdot\boldsymbol{\pi})V(\boldsymbol{\sigma}\cdot\boldsymbol{\pi})$ respectively, represented in the RMB condition.

The **M** matrix (Eq. (7)) includes the kinetic energy, angular momentum, and electric quadrupole integrals evaluated in the GIAO basis. The **W** matrix (Eq. (8)) includes relativistic effects, *e.g.*, spin-free and spin-orbit and their interactions with the magnetic field. Equations (7) and (8) can be separated using the Dirac identity into the following expressions:

$$\frac{1}{2}(\boldsymbol{\sigma}\cdot\boldsymbol{\pi})(\boldsymbol{\sigma}\cdot\boldsymbol{\pi}) = -\frac{1}{2}\boldsymbol{\nabla}^2 + \frac{1}{2}(\boldsymbol{\sigma} - i\mathbf{r}\times\boldsymbol{\nabla})\cdot\mathbf{B} + \frac{1}{8}(\mathbf{B}\times\mathbf{r})^2 \tag{9}$$

$$\begin{aligned}(\boldsymbol{\sigma}\cdot\boldsymbol{\pi})V(\boldsymbol{\sigma}\cdot\boldsymbol{\pi}) &= (\boldsymbol{\sigma}\cdot\mathbf{p})V(\boldsymbol{\sigma}\cdot\mathbf{p}) + (\mathbf{p}V\cdot\mathbf{A} + \mathbf{A}V\cdot\mathbf{p}) \\ &\quad + i\boldsymbol{\sigma}\cdot(\mathbf{p}V\times\mathbf{A} + \mathbf{A}V\times\mathbf{p}) + \mathbf{A}V\cdot\mathbf{A}\end{aligned} \tag{10}$$

The static magnetic field **B** enters Eq. (10) as:

$$\begin{aligned}\mathbf{p}V\cdot\mathbf{A} + \mathbf{A}V\cdot\mathbf{p} = \frac{i}{2}\big\{&B_x[(\nabla_y V r_z + r_z V\nabla_y) - (\nabla_z V r_y + r_y V\nabla_z)] \\ &B_y[(\nabla_z V r_x + r_x V\nabla_z) - (\nabla_x V r_z + r_z V\nabla_x)] \\ &B_z[(\nabla_x V r_y + r_y V\nabla_x) - (\nabla_y V r_x + r_x V\nabla_y)]\big\}\end{aligned} \tag{11}$$

$$(\mathbf{p}V\times\mathbf{A} + \mathbf{A}V\times\mathbf{p})_\kappa = \sum_\mu \frac{1}{2}B_\mu(r_\kappa V p_\mu - p_\mu V r_\kappa) + \frac{1}{2}B_\kappa(p_\mu V r_\mu - r_\mu V p_\mu) \tag{12}$$

$$\begin{aligned}\mathbf{A}V\cdot\mathbf{A} &= xVx(B_y^2 + B_z^2) + yVy(B_x^2 + B_z^2) + zVz(B_x^2 + B_y^2) \\ &\quad - 2xVyB_xBy - 2yVzB_yB_z - 2xVzB_xB_z\end{aligned} \tag{13}$$

where $\kappa, \mu \in \{x, y, z\}$. For detailed integral evaluation algorithms for the **M** matrix, see Ref. 53. Integral evaluations for relativistic one-electron **W** matrix using GIAOs are non-trivial and details are presented in the Appendix.

The derivation of the X2C procedure under the RMB condition was presented in Ref. 35. Here, we include only the final expressions for completeness of the discussion. The two-component electron-only X2C Hamiltonian can be constructed as:

$$\mathbf{H}_{\mathrm{X2C}} = (\mathbf{K}^{-1})^{\dagger}\mathbf{R}^{\dagger}\{\mathbf{K}^{\dagger}V\mathbf{K} + c\sqrt{2\mathbf{t}}\mathbf{X} + \mathbf{X}c\sqrt{2\mathbf{t}} + \mathbf{X}^{\dagger}[\sqrt{2\mathbf{t}}^{-1}\mathbf{K}^{\dagger}(\boldsymbol{\sigma}\cdot\boldsymbol{\pi})V(\boldsymbol{\sigma}\cdot\boldsymbol{\pi})\mathbf{K}\sqrt{2\mathbf{t}}^{-1} - 2c^2]\mathbf{X}\}\mathbf{R}\mathbf{K}^{-1} \tag{14}$$

$$\mathbf{X} = \mathbf{C}'^{+}_{S}(\mathbf{C}'^{+}_{L})^{-1} \tag{15}$$

$$\mathbf{R} = (\mathbf{I} + \mathbf{X}^{\dagger}\mathbf{X})^{-\frac{1}{2}} \tag{16}$$

where the two-component matrix $\mathbf{K}$ is obtained by solving the following eigenvalue equation:

$$\mathbf{M}\mathbf{K} = \mathbf{S}\mathbf{K}\mathbf{t} \tag{17}$$

and $\mathbf{t}$ is the diagonal matrix of the eigenvalues.

The X2C Hamiltonian under the RMB condition, as shown in Eq. (14), allows for the variational inclusion of magnetic field perturbations in the Dirac equation. This ensures that the solution is bounded from below within the X2C formalism, enabling the application of variational procedures to obtain the ground state wave function in the presence of a magnetic field.

2.2.3 GIAO-X2C-CASSCF

The extension of the GIAO-X2C framework in the RMB condition to spinor-based CASSCF is straightforward, especially when only the non-relativistic or bare Coulomb operator is used for electron repulsion interaction in the X2C correlation calculations.[53] The process involves utilizing electron repulsion integrals with the finite field GIAOs (GIAO-ERI)[53] in X2C-CASSCF,[80] both of which have been previously developed.

However, the inclusion of a magnetic field breaks the time-reversal symmetry. Consequently, all components of the GIAO-X2C-CASSCF method—including atomic orbital (AO)

integrals, AO to spinor transformation, CASSCF orbital rotation, and eigensolvers—must be formulated in the Kramers' unrestricted framework.

Since orbital rotation in X2C-CASSCF directly modifies the orbital coefficients and the orbital coefficients enter the X2C transformation (see Eq. (15)), this typically requires the reconstruction and application of the transformation matrix at every X2C-CASSCF step due to the two-electron picture-change effect. However, the use of the approximate one-electron X2C approach within the one-electron four-component Dirac–Hartree–Fock framework[81] eliminates the need to recompute the two-component transformation matrix in the current implementation. This is because the two-electron operator is not transformed, ignoring the two-electron picture-change effect; therefore, the one-electron X2C transformation only depends on the four-component one-electron operator, which does not need to be solved self-consistently.

3 Computational Details

The geometries of 2,2,6,6-tetramethylcyclohexanone and pyrimidine were optimized with the B3LYP functional[82–85] with a 6-31G(d) basis set[86,87] in zero field, using the GAUSSIAN 16 computational chemistry software package.[88] See the Supporting Information for optimized structures. GIAO-6-31G(d) basis set is used for 2,2,6,6-tetramethylcyclohexanone and pyrimidine. GIAO-Sapporo-DKH3-DZP-2012-All[89] and GIAO-x2c-TZVPall-2c[90] basis sets are used for Mn^{2+} and $Mn(II)O_4^{6-}$, respectively. Computed spectra are broadened with a normalized Gaussian function

$$f_J(\omega) = \frac{1}{\sqrt{\pi}\sigma_J} \exp\left[-\left(\frac{\omega - \omega_{0J}}{\sigma_J}\right)^2\right] \tag{18}$$

where σ_J is broadening factor for state J and ω_{0J} is excitation energy. All GIAO-X2C-CASSCF calculations in finite magnetic field were performed in a development version of CHRONUS QUANTUM open source package.[91,92]

4 Benchmark and Discussion

4.1 Oxygen K-edge XMCD of 2,2,6,6-Tetramethylcyclohexanone

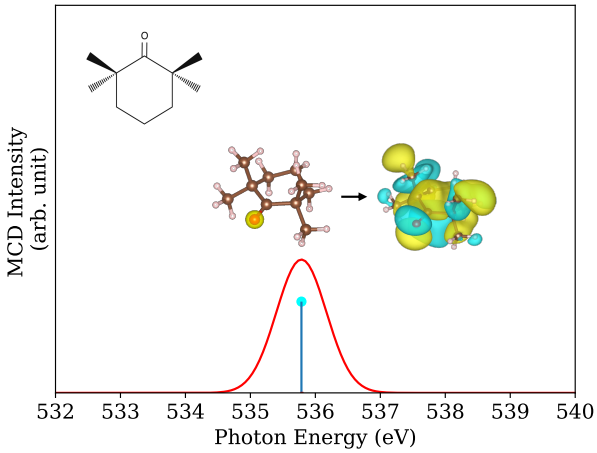

Figure 1. Simulated isotropic oxygen K-edge XMCD spectrum of 2,2,6,6-tetramethylcyclohexanone in a 2.106×10^{-5} a.u. ($\sim$ 4.95 T) magnetic field. Broadening factor is set to $\sigma = 0.015$ Hartree. Main molecular orbital contributions are shown.

The first benchmark case involves the organic molecule 2,2,6,6-tetramethylcyclohexanone. Since neither the ground state nor the excited state of this molecule exhibits Zeeman splitting, the XMCD should exhibit the same features as observed in the UV/Vis MCD spectrum, serving as an indirect way to validate the method. The oxygen K-edge XMCD probes the $1s \rightarrow \pi^*$ transition. For this system, we considered an active space of (2e, 4o), including two occupied oxygen $1s$ orbital and two unoccupied π^* orbital to provide a minimal description of the core excitation. The ground state and the lowest singlet excited state are included in the state-average orbital optimization. A magnetic field of 2.106×10^{-5} a.u. (approximately 4.95 T) is applied. The simulated oxygen K-edge XMCD spectrum of 2,2,6,6-tetramethylcyclohexanone is shown in Figure 1. The computed oxygen K-edge XMCD band is located at 535.8 eV, corresponding to the $1s \rightarrow \pi^*$ transition, and exhibits similar characteristics to those observed in the UV/Vis MCD spectrum.[93]

4.2 Nitrogen K-edge XMCD of Pyrimidine

The system of pyrimidine is a more complicated system than 2,2,6,6-tetramethylcyclohexanone as both UV/Vis MCD and nitrogen K-edge XMCD consist of multiple excitations. For UV/Vis MCD, we mainly consider four lowest excitations involving $^1B_1(n \to \pi^*)$, $^1B_2(\pi \to \pi^*)$, $^2B_1(n \to \pi^*)$ and $^1A_1(\pi \to \pi^*)$, resulting in an (8e, 12o) active space for the MCD calculation. The reference orbitals for the MCD calculation were optimized with a state-average scheme using all states. For the nitrogen K-edge XMCD calculation, four nitrogen $1s$ orbitals were added to the active space. The ground state and all 880 states, which contribute to the nitrogen K-edge spectrum, are considered in state-averaged orbital optimization in the (12e, 16o) active space for the XMCD calculation. A magnetic field of 2.238×10^{-5} a.u. (~ 5.26 T) is applied.

The simulated MCD and XMCD spectra are shown in Figure 2. The peaks of the computed MCD band are located at 3.38, 5.61, 5.68 and 6.40 eV, after applying a uniform shift of 2.15 eV. The signs of the computed UV/Vis MCD peaks are in agreement with experiments.[94,95] For nitrogen K-edge excitations, the $1s$ core orbitals of two different N atoms are linearly transformed to symmetric a_1 and anti-asymmetric b_2 molecular orbitals. The simulated XMCD spectra is shown in Figure 2(b). Two main positive peaks are observed. The first peak is located at 401.4 eV, arising from the $a_1 \to \pi^*$ and $b_2 \to \pi^*$ transition. The second peak at 412.4 eV has a complex electronic structure. Projecting the reduced density onto the orbital space reveals that these are shake-up peaks[4,5] which are two-electron excitations including one-electron nitrogen K-edge $a_1 \to \pi^*$ or $b_2 \to \pi^*$ mixed with a second-electron $n \to \pi^*$ or $\pi \to \pi^*$ transitions.

4.3 L-edge XMCD of Mn^{2+} ion

In this study, we investigate the L-edge XMCD spectrum of a high-spin Mn^{2+} ion. L-edge spectroscopy involves the excitation of electrons from the $2p$ core orbitals, which split into $p_{1/2}$ and $p_{3/2}$ manifolds due to spin-orbit coupling. The ground state of Mn^{2+} has a d^5

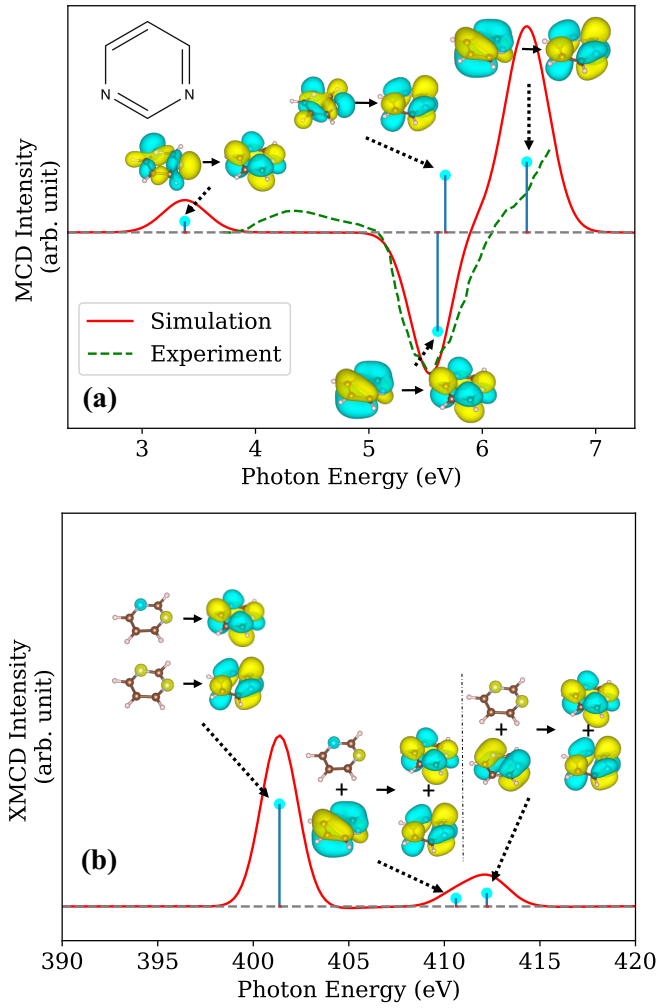

Figure 2. Simulated isotropic MCD (a) and nitrogen K-edge XMCD (b) spectrum of pyrimidine in a 2.238×10^{-5} a.u. magnetic field. Broadening factor is set to $\sigma = 0.01$ for MCD and $\sigma = 0.05$ Hartree for XMCD. Main molecular orbital contributions are shown. A uniform shift of 2.15 eV is applied to the computed MCD spectrum. MCD experimental results were reproduced from Ref. 94. Copyright 1977 American Chemical Society.

high-spin configuration, where the $3d$ orbitals are split into degenerate six-fold $d_{5/2}$ and four-fold $d_{3/2}$ groups. When an external magnetic field is applied, the degenerate orbitals split into $2J+1$ microstates ($m_J = -J, ..., J$), shown in Figure 3. These microstates, with well-defined magnetic moments, make the free Mn^{2+} ion an ideal test case for studying the XMCD selection rules.

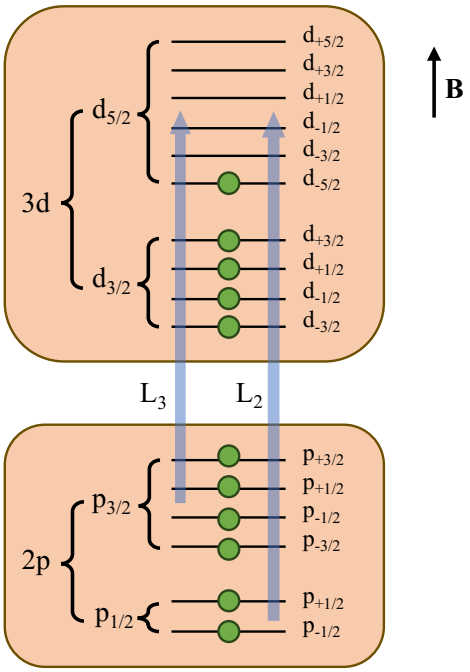

Figure 3. Energy diagram of of Mn^{2+} in finite magnetic field.

We selected all six core $2p$ and ten valence $3d$ spinor orbitals in an (11e, 16o) active space for GIAO-X2C-CASSCF calculations. The state-averaged orbital optimization considered 6 ground microstates and 1260 single-electron excited states resulting from $2p \rightarrow 3d$ transitions. To compute the XMCD spectrum, we obtained a total of 1512 states for the computation of transition dipoles. It is important to note that the sign of XMCD is defined differently in various literature sources. For the XMCD spectrum at the L-edge of the Mn^{2+} ion and the $Mn(II)O_4^{6-}$ complex (discussed in the next section), a phase factor of -1 is added to Equation (4) to match the convention where the L_3 peak is negative.[11]

The GIAO-X2C-CASSCF simulated L-edge XMCD spectrum is shown in Figure 4. In

the absence of an external magnetic field, the L_3 and L_2 peaks arise from $p_{3/2} \rightarrow d_{5/2}$ and $p_{1/2} \rightarrow d_{3/2}$, respectively, from the single-electron orbital picture, resulting in two single peaks in the L-edge spectrum. In XMCD, the external filed splits both the $2p$ and $3d$ orbitals into non-degenerate manifolds (see Figure 3), giving rise to additional peaks observed in the L-edge spectrum. There are seven main peaks, labeled **1** to **7**, in the computed XMCD spectrum. By analyzing the configuration interaction coefficients and m_J values of the molecular orbitals, we can identify the nature of these peaks, as shown in Figure 4.

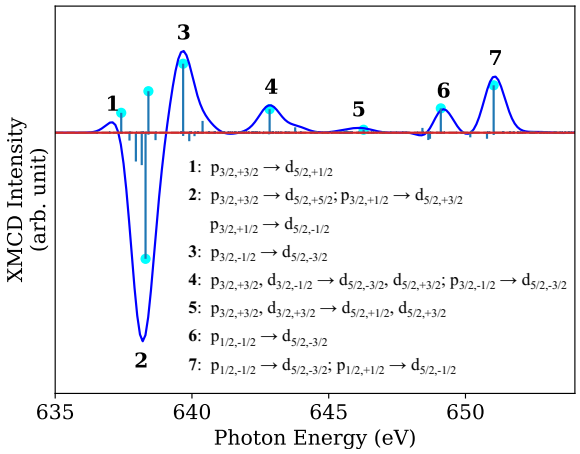

Figure 4. Simulated L-edge XMCD spectrum of Mn^{2+} in an 8 T magnetic field. The broadening factor is set to $\sigma = 0.02$ Hartree. Main peaks are labeled with their corresponding electronic transitions.

In the following discussion, we use the notation of l_{J,m_J} to identify allowed XMCD transitions. The peaks at 637-647 eV feature the L_3 edge, composed of five main peaks labeled **1** to **5**. Generally, these peaks arise primarily from excitations from the $p_{3/2}$ to the $d_{5/2}$ sublevels. The peaks at 647-652 are the L_2 edge, consisting of transitions from $p_{1/2}$ to $d_{5/2}$ orbitals.

The first small peak, **1**, near 637 eV originates from the excitation $p_{3/2,+3/2} \rightarrow d_{5/2,+1/2}$. The total change in m_J is -1, indicating that this excitation is RCP-active and will result in a positive peak. The large negative peak, **2**, near 638 eV, includes two main negative contributions: $p_{3/2,+1/2} \rightarrow d_{5/2,+3/2}$ and $p_{3/2,+3/2} \rightarrow d_{5/2,+5/2}$. Since $\Delta m_J = +1$, these

excitations are LCP-active and result in a negative peak. There is also a positive contribution from $p_{3/2,+1/2} \rightarrow d_{5/2,-1/2}$ near 638 eV. However, this positive feature cannot be observed due to the dominant negative intensity from the other transitions. The positive peak **3** at ~639 eV includes the $p_{3/2,-1/2} \rightarrow d_{5/2,-3/2}$ transition, giving rise to a derivative line shape of the L_3 edge.

Peaks **4** and **5** are L-edge shake-up transitions.[4] Peak **4** arises from a double excitation $p_{3/2,+3/2}, d_{3/2,-1/2} \rightarrow d_{5/2,-3/2}, d_{5/2,+3/2}$. Similarly, peak **5** consists of another double excitation $p_{3/2,+3/2}, d_{3/2,+3/2} \rightarrow d_{5/2,+1/2}, d_{5/2,+3/2}$. These shake-up peaks cannot be observed using the linear-response TDDFT approach because they feature a core-electron transition accompanied with a d-d transition. Both double excitations result in $\Delta m_J = -1$, making them RCP-active and giving rise to positive peaks.

Peaks **6** and **7** feature the L_2 edge. Unlike peaks **1** to **5**, the main excitations of peaks **6** and **7** originate from the $p_{1/2}$ manifold. For peak **6**, the excitation is $p_{1/2,-1/2} \rightarrow d_{5/2,-3/2}$. Peak **7** consists of two excitations: $p_{1/2,+1/2} \rightarrow d_{5/2,-1/2}$ and $p_{1/2,-1/2} \rightarrow d_{5/2,-3/2}$. All excitations in peaks **6** and **7** are associated with $\Delta m_J = -1$, showing positive RCP-activities.

4.4 Temperature-Dependent L-edge XMCD of T_d Mn(II)O_4^{6-}

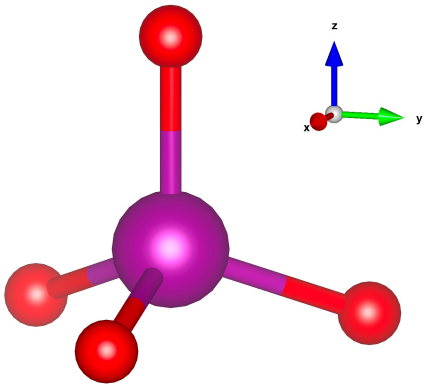

Figure 5. Molecular structure of T_d Mn(II)O_4^{6-}. An 8 T magnetic field is applied to the $+z$ direction.

Temperature-dependent Mn L-edge XMCD of Mn^{2+}-doped ZnO has been measured ex-

perimentally to study the magnetic properties of the material.[96–98] We simulate the spectrum using a tetrahedrally coordinated $Mn(II)O_4^{6-}$ cluster with the Mn-O bond length set to the experimental value of 2 Å.[99] For the GIAO-X2C-CASSCF calculations, we used the same active space setup as in the free Mn^{2+} ion case, with the magnetic field aligned to the $+z$ direction (See Figure 5).

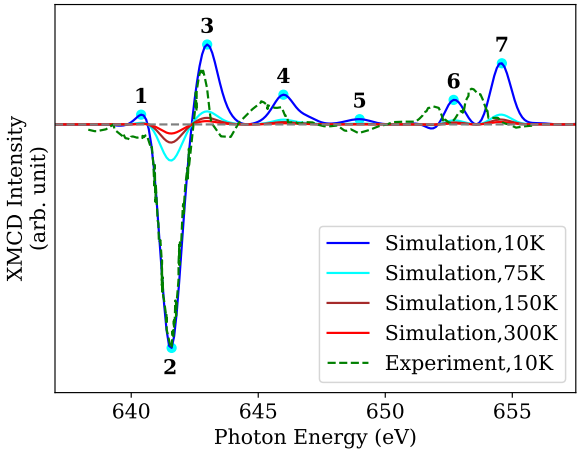

Figure 6. Experimental and simulated XMCD spectrum of $Mn(II)O_4^{6-}$ L_2 and L_3 transitions in an 8 T magnetic field. The broadening factor is set to $\sigma = 0.02$ Hartree. The main peaks are marked. Experimental results were reproduced from Ref. 98, with the permission of AIP Publishing. The computed peaks are blue-shifted by 5.59 eV to match the first largest experimental peak.

The GIAO-X2C-CASSCF simulated XMCD spectra in Figure 6 show an excellent agreement with experiment.[96–98] Similar to those in the L-edge XMCD spectrum of Mn^{2+}, 7 main peaks are observed. Like in the Mn^{2+} ion, the $Mn(II)O4^{6-}$ L-edge spectrum arises from Mn $2p$ core electron excitations. The splitting of the core electron $2p$ orbitals can still be described by $p_{1/2}$ and $p_{3/2}$ manifolds, as they are not strongly affected by the tetrahedral ligand field. The tetrahedral oxygen ligand field in $Mn(II)O4^{6-}$ splits the Mn $3d$ orbitals into e and t_2 levels. The high-spin configuration $e^2t_2^3$ gives rise to six-fold degenerate $E_{5/2}$ ground states. Due to the magnetic Zeeman effect, this six-fold degeneracy splits into non-degenerate microstates ($M_J = \pm\frac{1}{2}, \pm\frac{3}{2}, \pm\frac{5}{2}$). While the complete term symbol analysis of the final states in the Mn L-edge XMCD of $Mn(II)O_4^{6-}$ is complex, it is evident that the key

features and transitions can be understood in terms of $p_{1/2}$ and $p_{3/2}$ transitions into these microstates, similar to those in the free Mn^{2+} ion.

Unlike single-reference-based methods, the GIAO-X2C-CASSCF approach is capable of resolving all microstates ($M_J = \pm\frac{1}{2}, \pm\frac{3}{2}, \pm\frac{5}{2}$) and the XMCD transitions originating from each of them. At temperatures above 0 K, higher-energy microstates can be populated according to the Boltzmann distribution, resulting in temperature-dependent MCD spectra. Figure 6 shows the XMCD spectral progression from 10 K to 300 K. As higher-energy microstates become occupied, the probabilities of promoting $2p$ electrons to these levels decrease. The computed spectral progression accurately reflects the reduced intensities of XMCD peaks at higher temperatures.

5 Conclusion

In this work, we have developed the exact-two-component complete state-average active space self-consistent-field (X2C-CASSCF) approach that incorporates a non-perturbative treatment of static magnetic fields using gauge-including atomic orbitals (GIAOs). The GIAO-X2C-CASSCF methodology effectively captures all microstates within the same $2J+1$-degenerate manifold and their splitting in a static magnetic field, which are not accessible through single-reference-based methods.

We introduced the restricted-magnetic-balance condition for the four- to two-component transformation in a static magnetic field, enabling the variational inclusion of the magnetic field in two-component electronic structure theory. Additionally, we derived recursive expressions for evaluating one-electron relativistic integrals using gauge-including atomic orbitals in the presence of a finite magnetic field.

The relativistic GIAO-X2C-CASSCF was tested in simulating oxygen and nitrogen X-ray K-edge MCD spectroscopy for organic compounds such as 2,2,6,6-tetramethylcyclohexanone and pyrimidine. Additionally, we simulated L-edge X-ray MCD spectroscopy for high-spin

open-shell transition metal ion Mn^{2+}, as well as temperature-dependent X-ray MCD spectroscopy for tetrahedral $Mn(II)O_4^{6-}$. For Mn^{2+}, the origins and selection rules of $L_{2,3}$ XMCD transitions were demonstrated with a careful analysis of configurations and atomic orbitals. The computed $Mn(II)O_4^{6-}$ L-edge XMCD spectrum agrees well with experiment.

We have shown that the GIAO-X2C-CASSCF method is highly effective tool for simulating MCD and XMCD spectra for systems with high multiplicity. However, the CASSCF method lacks a description of dynamic electron correlation. This can be rectified by further corrections to excitation energies using methods such as MRCI, MRPDFT, or MRPT2.[39,77,78]

Acknowledgement

The development of the computational magnetic circular dichroism method is supported by the National Science Foundation through Grant No. CHE-2154346. The advancement of variational relativistic multi-reference methods is funded by the U.S. Department of Energy, Office of Science, Basic Energy Sciences, within the Heavy-Element Chemistry program (Grant No. DE-SC0021100). The Chronus Quantum computational software development is supported by the Office of Advanced Cyberinfrastructure, National Science Foundation (Grant No. OAC-2103717).

Supporting Information Available

Optimized structures of 2,2,6,6-tetramethylcyclohexanone and pyrimidine.

Appendix: Evaluation of One-Electron Relativistic Integrals with Finite-Magnetic-Field Gauge-Including Atomic Orbitals

A complex-valued finite-field gauge-including atomic orbital (GIAO) is defined as

$$\tilde{\chi}(\mathbf{r}-\mathbf{R}_A;\mathbf{k}_A) = \chi(\mathbf{r}-\mathbf{R}_A)e^{i\mathbf{k}_A\cdot(\mathbf{r}-\mathbf{R}_A)} \tag{19}$$

where $\{\chi\}$ are atom-centered Gaussian type orbitals,

$$\chi = (x-R_x)^{a_x}(y-R_y)^{a_y}(z-R_z)^{a_z}e^{-\zeta|\mathbf{r}-\mathbf{R}_A|^2} \tag{20}$$

$$|\mathbf{r}-\mathbf{R}| = \sqrt{(x-R_x)^2+(y-R_y)^2+(z-R_z)^2} \tag{21}$$

$\mathbf{R} = \{R_x, R_y, R_z\}$ is the coordinate of the atom center and $\mathbf{a} = \{a_x, a_y, a_z\}$ is the angular momentum. ζ is the exponent of primitive Gaussian type orbitals. In the following discussion, we denote the angular momentum of the basis functions by $\mathbf{a}$ and $\mathbf{b}$, and use a tilde ($\tilde{\mathbf{a}}$ and $\tilde{\mathbf{b}}$) to indicate that the orbitals are complex-valued finite-field GIAO.

The one-electron relativistic integrals are used in the one-electron X2C Hamiltonian. Based on Eqs. (11) and (12), three types of integrals are needed, all involving the electron-nuclear Coulomb operator $V = -\frac{1}{|\mathbf{r}-\mathbf{R}|}$:

- Spin-free $(\tilde{\mathbf{a}}|\mathbf{p}V\cdot\mathbf{p}|\tilde{\mathbf{b}})$ and spin-orbit $(\tilde{\mathbf{a}}|\mathbf{p}V\times\mathbf{p}|\tilde{\mathbf{b}})$ integrals, which have two derivative operators and one nuclear potential operator.

- $(\tilde{\mathbf{a}}|\nabla_i V r_j|\tilde{\mathbf{b}})$ and $(\tilde{\mathbf{a}}|r_j V\nabla_i|\tilde{\mathbf{b}})$ integrals, which have one derivative operator, one Cartesian coordinate operator, and a nuclear potential operator.

- $(\tilde{\mathbf{a}}|\mathbf{A}V\cdot\mathbf{A}|\tilde{\mathbf{b}})$ integrals, which have two coordinate operators and a nuclear potential operator.

A.1 $(\tilde{\mathbf{a}}|\mathbf{p}V\cdot\mathbf{p}|\tilde{\mathbf{b}})$ Integral Evaluation

The derivative with respect to electronic degrees of freedom can be transformed into the derivative with respect to the nuclear coordinate

$$\begin{aligned}
&\frac{\partial}{\partial r_j}\tilde{\chi}(\mathbf{r}-\mathbf{R}_A;\mathbf{k}_A;\mathbf{a};\zeta) \\
&=-\frac{\partial}{\partial R_{A,j}}\tilde{\chi}(\mathbf{r}-\mathbf{R}_A;\mathbf{k}_A;\mathbf{a};\zeta) \\
&=-2\zeta\tilde{\chi}(\mathbf{r}-\mathbf{R}_A;\mathbf{k}_A;\mathbf{a}+\mathbf{1}_j;\zeta)+a_j\tilde{\chi}(\mathbf{r}-\mathbf{R}_A;\mathbf{k}_A;\mathbf{a}-\mathbf{1}_j;\zeta)+ik_{A,j}\tilde{\chi}(\mathbf{r}-\mathbf{R}_A;\mathbf{k}_A;\mathbf{a};\zeta) \\
&j\in\{x,y,z\}
\end{aligned} \tag{22}$$

For the $(\tilde{\mathbf{a}}|\mathbf{p}V\cdot\mathbf{p}|\tilde{\mathbf{b}})$ and spin-orbit $(\tilde{\mathbf{a}}|\mathbf{p}V\times\mathbf{p}|\tilde{\mathbf{b}})$ integrals, we can rewrite them as the second derivative of nuclear attraction integral with respect to nuclear coordinates,

$$(\tilde{\mathbf{a}}|\mathbf{p}V\cdot\mathbf{p}|\tilde{\mathbf{b}})=-(\tilde{\mathbf{a}}|\boldsymbol{\nabla}V\cdot\boldsymbol{\nabla}|\tilde{\mathbf{b}})=\sum_{j=x,y,z}\partial_{A_j}\partial_{B_j}(\tilde{\mathbf{a}}|V|\tilde{\mathbf{b}}) \tag{23}$$

$$\begin{aligned}
(\tilde{\mathbf{a}}|\mathbf{p}V\times\mathbf{p}|\tilde{\mathbf{b}})&=-(\tilde{\mathbf{a}}|\boldsymbol{\nabla}V\times\boldsymbol{\nabla}|\tilde{\mathbf{b}})=\sum_{i,j,k=x,y,z}\varepsilon_{ijk}\,\partial_{A_i}\partial_{B_j}(\tilde{\mathbf{a}}|V|\tilde{\mathbf{b}})\hat{k} \\
&i,j,k\in x,y,z
\end{aligned} \tag{24}$$

where $\hat{k}$ is the unit vector, and $\epsilon_{xyz,yzx,zxy}=1,\epsilon_{yzx,zyx,xzy}=-1$; otherwise 0.

According to Eq. (22), the second derivative can be evaluated in a recursive approach,

$$\begin{aligned}
\partial_{A_i}\partial_{B_j}(\tilde{\mathbf{a}}|V|\tilde{\mathbf{b}})=&2\zeta_a\{2\zeta_b(\tilde{\mathbf{a}}+\mathbf{1}_i|V|\tilde{\mathbf{b}}+\mathbf{1}_j)-b_j(\tilde{\mathbf{a}}+\mathbf{1}_i|V|\tilde{\mathbf{b}}-\mathbf{1}_j)-ik_{b,j}(\tilde{\mathbf{a}}+\mathbf{1}_i|V|\mathbf{b})\} \\
&-a_i\{2\zeta_b(\tilde{\mathbf{a}}-\mathbf{1}_i|V|\tilde{\mathbf{b}}+\mathbf{1}_j)-b_j(\tilde{\mathbf{a}}-\mathbf{1}_i|V|\tilde{\mathbf{b}}-\mathbf{1}_j)-ik_{b,j}(\tilde{\mathbf{a}}-\mathbf{1}_i|V|\tilde{\mathbf{b}})\} \\
&-ik_{a,i}\{2\zeta_b(\tilde{\mathbf{a}}|V|\tilde{\mathbf{b}}+\mathbf{1}_j)-b_j(\tilde{\mathbf{a}}|V|\tilde{\mathbf{b}}-\mathbf{1}_j)-ik_{b,j}(\tilde{\mathbf{a}}|V|\tilde{\mathbf{b}})\}
\end{aligned} \tag{25}$$

A.2 $(\tilde{\mathbf{a}}|\nabla_i V r_j|\tilde{\mathbf{b}})$ Integral Evaluation

For the $(\tilde{\mathbf{a}}|\nabla_i V r_j|\tilde{\mathbf{b}})$ integral type, we use $r_i = (r_i - B_i) + B_i$ so that the derivative can be written as

$$\begin{aligned}(\tilde{\mathbf{a}}|\nabla_i V r_j|\tilde{\mathbf{b}}) =& -(\nabla_i \tilde{\mathbf{a}}|V r_j|\tilde{\mathbf{b}}) = (\nabla_{A_i}\tilde{\mathbf{a}}|V r_j|\tilde{\mathbf{b}}) \\ =& 2\zeta_a(\tilde{\mathbf{a}}+\mathbf{1}_i|V|\tilde{\mathbf{b}}+\mathbf{1}_j) + B_j(\tilde{\mathbf{a}}+\mathbf{1}_i|V|\tilde{\mathbf{b}})] \\ & - a_i[(\tilde{\mathbf{a}}-\mathbf{1}_i|V|\tilde{\mathbf{b}}+\mathbf{1}_j) + B_j(\tilde{\mathbf{a}}-\mathbf{1}_i|V|\tilde{\mathbf{b}})] \\ & - ik_{a,i}[(\tilde{\mathbf{a}}|V|\tilde{\mathbf{b}}+\mathbf{1}_j) + B_j(\tilde{\mathbf{a}}|V|\tilde{\mathbf{b}})] \end{aligned} \tag{26}$$

Similarly, we have

$$\begin{aligned}(\tilde{\mathbf{a}}|r_j V\nabla_i|\tilde{\mathbf{b}}) =& -[2\zeta_b(\tilde{\mathbf{a}}+\mathbf{1}_j|V|\tilde{\mathbf{b}}+\mathbf{1}_i) - N_\alpha(\mathbf{b})(\tilde{\mathbf{a}}+\mathbf{1}_j|V|\tilde{\mathbf{b}}-\mathbf{1}_i) - ik_{b,i}(\tilde{\mathbf{a}}+\mathbf{1}_j|V|\tilde{\mathbf{b}})] \\ & - A_j[2\zeta_b(\tilde{\mathbf{a}}|V|\tilde{\mathbf{b}}+\mathbf{1}_\alpha) - b_i(\tilde{\mathbf{a}}|V|\tilde{\mathbf{b}}-\mathbf{1}_i) - ik_{b,i}(\tilde{\mathbf{a}}|V|\tilde{\mathbf{b}})] \end{aligned} \tag{27}$$

Notice that linear combinations of Eq. (26) and Eq. (27) lead to Hermitian $\nabla_j V r_i - r_i V\nabla_j$ and anti-Hermitian $r_i V\nabla_j + \nabla_j V r_i$.

A.3 $(\tilde{\mathbf{a}}|\mathbf{A}V\cdot\mathbf{A}|\tilde{\mathbf{b}})$ Integral Evaluation

To evaluate the $(\tilde{\mathbf{a}}|\mathbf{A}V\cdot\mathbf{A}|\tilde{\mathbf{b}})$ integral, we use the operator in the form of Eq. (13), where the integral of the type $(\tilde{\mathbf{a}}|r_i V r_j|\tilde{\mathbf{b}})$ can be evaluated as

$$\begin{aligned}(\tilde{\mathbf{a}}|r_i V r_j|\tilde{\mathbf{b}}) &= (\tilde{\mathbf{a}}|[(r-A)_i + A_i]V[(r-B)_j + B_j]|\tilde{\mathbf{b}}) \\ &= (\tilde{\mathbf{a}}+\mathbf{1}_i|V|\tilde{\mathbf{b}}+\mathbf{1}_j) + B_j(\tilde{\mathbf{a}}+\mathbf{1}_i|V|\tilde{\mathbf{b}}) + A_i(\tilde{\mathbf{a}}|V|\tilde{\mathbf{b}}+\mathbf{1}_j) + A_i B_j(\tilde{\mathbf{a}}|V|\tilde{\mathbf{b}}) \end{aligned} \tag{28}$$

A.4 Evaluation of Nuclear Attraction Integral with Finite-Width Nucleus and Finite Mangetic Field GIAO

For relativistic calculations, a Gaussian charge distribution of the nucleus is utilized.[100] In the finite width nuclear model, the nuclear potential is given by:

$$V(\mathbf{r}) = -\int d^3\mathbf{R} \quad \frac{N_c e^{-\zeta_c(\mathbf{R}-\mathbf{C})^2}}{|\mathbf{r}-\mathbf{R}|} \tag{29}$$

where $e^{-\zeta_c(\mathbf{R}-\mathbf{C})^2}$ represents the Gaussian distribution of the charge with the nucleus centered at $\mathbf{C}$. The parameter ζ_c determines the diffusivity of the nucleus. The normalization condition is

$$\int d^3\mathbf{R}\, N_c e^{-\zeta_c(\mathbf{R}-\mathbf{C})^2} = Z_c \tag{30}$$

where Z_c is the nuclear charge.

The electron-nuclear attraction integral with finite-width nuclear model can be viewed as a special case of electron repulsion integral,

$$\begin{aligned}(\tilde{\mathbf{a}}|V(\mathbf{r})|\tilde{\mathbf{b}}) &= \iint d^3\mathbf{R} d^3\mathbf{r} \tilde{\chi}_a(\mathbf{r})\tilde{\chi}_b(\mathbf{r}) \frac{N_c e^{-\zeta_c(\mathbf{R}-\mathbf{C})^2}}{|\mathbf{r}-\mathbf{R}|} \\ &= \iint d^3\mathbf{R} d^3\mathbf{r} \tilde{\chi}_a(\mathbf{r})\tilde{\chi}_b(\mathbf{r}) \frac{1}{|\mathbf{r}-\mathbf{R}|} \chi_c(\mathbf{R})\chi_d(\mathbf{R})\end{aligned} \tag{31}$$

where

$$\chi_c = N_c e^{-\zeta_c(\mathbf{R}-\mathbf{C})^2}, \qquad \chi_d = 1 = e^0 \tag{32}$$

χ_c and χ_d are Gaussian orbitals instead of London orbitals.

We define

$$\zeta = \zeta_a + \zeta_b, \tag{33}$$

$$\rho = \frac{\zeta\zeta_c}{\zeta + \zeta_c} \tag{34}$$

$$\mathbf{P} = \frac{\zeta_a\mathbf{A} + \zeta_b\mathbf{B}}{\zeta} \tag{35}$$

$$\mathbf{W} = \frac{\zeta\mathbf{P} + \zeta_c\mathbf{C}}{\zeta + \zeta_c} \tag{36}$$

$$\mathbf{k}_p = -\mathbf{k}_a + \mathbf{k}_b \tag{37}$$

$$\mathbf{k}_q = \mathbf{0} \tag{38}$$

By substituting these quantities into the recursion of the electron repulsion integral using GIAO as described in Ref. 53, and following some mathematical derivations, we obtain a recursive expression for the nuclear attraction integral with a finite-width nuclear model and finite magnetic field GIAO:

$$\begin{aligned}((\tilde{\mathbf{a}} + \mathbf{1}_i)|V|\tilde{\mathbf{b}})^{(m)} =&(P_i + \frac{ik_{p,i}}{2\zeta} - A_i)(\tilde{\mathbf{a}}|V|\tilde{\mathbf{b}})^{(m)} - (P_i + \frac{ik_{p,i}}{2\zeta} - C_i)(\tilde{\mathbf{a}}|V|\tilde{\mathbf{b}})^{(m+1)} \\ &+\frac{1}{2\zeta}N_i(\mathbf{a})\big\{((\tilde{\mathbf{a}} - \mathbf{1}_i)|V|\tilde{\mathbf{b}})^{(m)} - ((\tilde{\mathbf{a}} - \mathbf{1}_i)|V|\tilde{\mathbf{b}})^{(m+1)}\big\} \\ &+\frac{1}{2\zeta}N_i(\mathbf{b})\big\{(\tilde{\mathbf{a}}|V|(\tilde{\mathbf{b}} - \mathbf{1}_i))^{(m)} - (\tilde{\mathbf{b}}|V|(\tilde{\mathbf{a}} - \mathbf{1}_i))^{(m+1)}\big\}\end{aligned} \tag{39}$$

The GIAO auxiliary integral is

$$(\tilde{\mathbf{0}}|V|\tilde{\mathbf{0}})^{(m)} = Z_c(\tilde{\mathbf{0}}||\tilde{\mathbf{0}})\left(\frac{\zeta_c}{\zeta + \zeta_c}\right)^m 2\left(\frac{\rho}{\pi}\right)^{1/2} F_m(T) \tag{40}$$

where T in the Boys function has the following definition

$$T = \rho\left(\mathbf{P} - \mathbf{C} + i\frac{\mathbf{k}_p}{2\zeta}\right)^2 \tag{41}$$

References

(1) Piepho, S.; Schatz, P. *Group Theory in Spectroscopy: With Applications to Magnetic Circular Dichroism*; Wiley, 1983.

(2) Mason, W. R. *A Practical Guide to Magnetic Circular Dichroism Spectroscopy*; John Wiley & Sons, Ltd, 2007; Chapter 1, pp 1–3.

(3) Barron, L. D. *Molecular Light Scattering and Optical Activity*; Cambridge University Press, 2009.

(4) Kasper, J. M.; Stetina, T. F.; Jenkins, A. J.; Li, X. Ab Initio Methods for L-edge X-ray Absorption Spectroscopy. *Chem. Phys. Rev.* **2020**, *1*, 011304.

(5) Ehrman, J. N.; Shumilov, K.; Jenkins, A. J.; Kasper, J. M.; Vitova, T.; Batista, E. R.; Yang, P.; Li, X. Unveiling Hidden Shake-Up Features in the Uranyl M_4-Edge Spectrum. *JACS Au* **2024**, *4*, 1134–1141.

(6) Shumilov, K. D.; Jenkins, A. J.; La Pierre, H. S.; Vlaisavljevich, B.; Li, X. Overdestabilization vs Overstabilization in the Theoretical Analysis of f-Orbital Covalency. *J. Am. Chem. Soc.* **2024**, *146*, 12030–12039.

(7) Thole, B. T.; Carra, P.; Sette, F.; van der Laan, G. X-Ray Circular Dichroism as a Probe of Orbital Magnetization. *Phys. Rev. Lett.* **1992**, *68*, 1943–1946.

(8) Carra, P.; Thole, B. T.; Altarelli, M.; Wang, X. X-Ray Circular Dichroism and Local Magnetic Fields. *Phys. Rev. Lett.* **1993**, *70*, 694–697.

(9) Stöhr, J. Exploring the Microscopic Origin of Magnetic Anisotropies With X-Ray Magnetic Circular Dichroism (XMCD) Spectroscopy. *J. Magn. Magn. Mater.* **1999**, *200*, 470–497.

(10) Funk, T.; Deb, A.; George, S. J.; Wang, H.; Cramer, S. P. X-Ray Magnetic Circular Dichroism – a High Energy Probe of Magnetic Properties. *Coord. Chem. Rev.* **2005**, *249*, 3–30.

(11) van der Laan, G.; Figueroa, A. I. X-Ray Magnetic Circular Dichroism – A Versatile Tool to Study Magnetism. *Coord. Chem. Rev.* **2014**, *277-278*, 95–129.

(12) Nelson, H. D.; Bradshaw, L. R.; Barrows, C. J.; Vlaskin, V. A.; Gamelin, D. R. Picosecond Dynamics of Excitonic Magnetic Polarons in Colloidal Diffusion-Doped $Cd_{1-x}Mn_xSe$ Quantum Dots. *ACS Nano* **2015**, *9*, 11177–11191.

(13) Barrows, C. J.; Vlaskin, V. A.; Gamelin, D. R. Absorption and Magnetic Circular Dichroism Analyses of Giant Zeeman Splittings in Diffusion-Doped Colloidal $Cd_{1-x}Mn_xSe$ Quantum Dots. *J. Phys. Chem. Lett.* **2015**, *6*, 3076–3081.

(14) Barrows, C. J.; Fainblat, R.; Gamelin, D. R. Excitonic Zeeman Splittings in Colloidal CdSe Quantum Dots Doped with Single Magnetic Impurities. *J. Mater. Chem. C* **2017**, *5*, 5232–5238.

(15) Rogalev, A.; Ollefs, K.; Wilhelm, F. *X-Ray Absorption and X-Ray Emission Spectroscopy*; John Wiley & Sons, Ltd, 2016; Chapter 23, pp 671–694.

(16) Pizzini, S.; Vogel, J.; Bonfim, M.; Fontaine, A. In *Spin Dynamics in Confined Magnetic Structures II*; Hillebrands, B., Ounadjela, K., Eds.; Springer Berlin Heidelberg: Berlin, Heidelberg, 2003; pp 157–187.

(17) van der Laan, G. Applications of Soft X-Ray Magnetic Dichroism. *J. Phys.: Conf. Ser.* **2013**, *430*, 012127.

(18) Takubo, K.; Yamamoto, K.; Hirata, Y.; Yokoyama, Y.; Kubota, Y.; Yamamoto, S.; Yamamoto, S.; Matsuda, I.; Shin, S.; Seki, T. et al. Capturing Ultrafast Magnetic

Dynamics by Time-Resolved Soft X-Ray Magnetic Circular Dichroism. *Appl. Phys. Lett.* **2017**, *110*, 162401.

(19) van der Laan, G. Time-Resolved X-Ray Detected Ferromagnetic Resonance of Spin Currents. *J. Electron Spectros. Relat. Phenomena* **2017**, *220*, 137–146.

(20) Sun, S.; Gu, B.; Hu, H.; Lu, L.; Tang, D.; Chernyak, V. Y.; Li, X.; Mukamel, S. Direct Probe of Conical Intersection Photochemistry by Time-Resolved X-ray Magnetic Circular Dichroism. *J. Am. Chem. Soc.* **2024**, *146*, 19863–19873.

(21) Coriani, S.; Jørgensen, P.; Rizzo, A.; Ruud, K.; Olsen, J. Ab Initio Determinations of Magnetic Circular Dichroism. *Chem. Phys. Lett.* **1999**, *300*, 61–68.

(22) Krykunov, M.; Seth, M.; Ziegler, T.; Autschbach, J. Calculation of the Magnetic Circular Dichroism B Term From the Imaginary Part of the Verdet Constant Using Damped Time-Dependent Density Functional Theory. *J. Chem. Phys.* **2007**, *127*, 244102.

(23) Solheim, H.; Ruud, K.; Coriani, S.; Norman, P. Complex Polarization Propagator Calculations of Magnetic Circular Dichroism Spectra. *J. Chem. Phys.* **2008**, *128*, 094103.

(24) Solheim, H.; Ruud, K.; Coriani, S.; Norman, P. The A and B Terms of Magnetic Circular Dichroism Revisited. *J. Phys. Chem. A* **2008**, *112*, 9615–9618.

(25) Seth, M.; Ziegler, T. Formulation of Magnetically Perturbed Time-Dependent Density Functional Theory. *J. Chem. Phys.* **2007**, *127*, 134108.

(26) Seth, M.; Krykunov, M.; Ziegler, T.; Autschbach, J.; Banerjee, A. Application of Magnetically Perturbed Time-Dependent Density Functional Theory to Magnetic Circular Dichroism: Calculation of B Terms. *J. Chem. Phys.* **2008**, *128*, 144105.

(27) Seth, M.; Krykunov, M.; Ziegler, T.; Autschbach, J. Application of Magnetically Perturbed Time-Dependent Density Functional Theory to Magnetic Circular Dichroism. II. Calculation of A Terms. *J. Chem. Phys.* **2008**, *128*, 234102.

(28) Ganyushin, D.; Neese, F. First-Principles Calculations of Magnetic Circular Dichroism Spectra. *J. Chem. Phys.* **2008**, *128*, 114117.

(29) Gendron, F.; Fleischauer, V. E.; Duignan, T. J.; Scott, B. L.; Löble, M. W.; Cary, S. K.; Kozimor, S. A.; Bolvin, H.; Neidig, M. L.; Autschbach, J. Magnetic Circular Dichroism of UCl_6^- in the Ligand-to-metal Charge-Transfer Spectral Region. *Phys. Chem. Chem. Phys.* **2017**, *19*, 17300–17313.

(30) Heit, Y. N.; Sergentu, D.-C.; Autschbach, J. Magnetic circular dichroism spectra of transition metal complexes calculated from restricted active space wavefunctions. *Phys. Chem. Chem. Phys.* **2019**, *21*, 5586–5597.

(31) Andersen, J. H.; Coriani, S.; Hättig, C. Efficient Protocol for Computing MCD Spectra in a Broad Frequency Range Combining Resonant and Damped CC2 Quadratic Response Theory. *J. Chem. Theory Comput.* **2023**, *19*, 5977–5987.

(32) Sun, S.; Williams-Young, D.; Li, X. An Ab Initio Linear Response Method for Computing Magnetic Circular Dichroism Spectra with Nonperturbative Treatment of Magnetic Field. *J. Chem. Theory Comput.* **2019**, *15*, 3162–3169.

(33) Stetina, T.; Sun, S.; Williams-Yong, D. B.; Li, X. Modeling Magneto-Photoabsorption Using Time-Dependent Complex Generalized Hartree-Fock. *ChemPhotoChem* **2019**, *3*, 739–746.

(34) Sun, S.; Beck, R.; Williams-Young, D. B.; Li, X. Simulating Magnetic Circular Dichroism Spectra with Real-Time Time-Dependent Density Functional Theory in Gauge Including Atomic Orbitals. *J. Chem. Theory Comput.* **2019**, *15*, 6824–6831.

(35) Sun, S.; Li, X. Relativistic Effects in Magnetic Circular Dichroism: Restricted Magnetic Balance and Temperature Dependence. *J. Chem. Theory Comput.* **2020**, *16*, 4533–4542.

(36) Pausch, A.; Holzer, C.; Klopper, W. Efficient Calculation of Magnetic Circular Dichroism Spectra Using Spin-Noncollinear Linear-Response Time-Dependent Density Functional Theory in Finite Magnetic Fields. *J. Chem. Theory Comput.* **2022**, *18*, 3747–3758.

(37) Holzer, C. Practical Post-Kohn-Sham Methods for Time-Reversal Symmetry Breaking References. *J. Chem. Theory Comput.* **2023**, *19*, 3131–3145.

(38) Jenkins, A. J.; Liu, H.; Kasper, J. M.; Frisch, M. J.; Li, X. Variational Relativistic Complete Active Space Self-Consistent Field Method. *J. Chem. Theory Comput.* **2019**, *15*, 2974–2982.

(39) Jenkins, A. J.; Hu, H.; Lu, L.; Frisch, M. J.; Li, X. Two-Component Multireference Restricted Active Space Configuration Interaction for the Computation of L-Edge X-ray Absorption Spectra. *J. Chem. Theory Comput.* **2022**, *18*, 141–150.

(40) Helgaker, T.; Taylor, P. R. *Modern Electronic Structure Theory*; pp 725–856.

(41) Ding, F.; Liang, W.; Chapman, C. T.; Isborn, C. M.; Li, X. On the Gauge Invariance of Nonperturbative Electronic Dynamics Using the Time-Dependent Hartree-Fock and Time-Dependent Kohn-Sham. *J. Chem. Phys.* **2011**, *135*, 164101.

(42) Lestrange, P. J.; Egidi, F.; Li, X. The Consequences of Improperly Describing Oscillator Strengths Beyond the Electric Dipole Approximation. *J. Chem. Phys.* **2015**, *143*, 234103.

(43) Epstein, S. T. Gauge Invariance of the Hartree-Fock Approximation. *J. Chem. Phys.* **1965**, *42*, 2897–2898.

(44) Epstein, S. T. Gauge Invariance, Current Conservation, and GIAO's. *J. Chem. Phys.* **1973**, *58*, 1592–1595.

(45) Gauss, J.; Stanton, J. F. Electron-Correlated Approaches for the Calculation of NMR Chemical Shifts. *Adv. Chem. Phys.* **2002**, 355–422.

(46) Schindler, M.; Kutzelnigg, W. Theory of Magnetic Susceptibilities and NMR Chemical Shifts in Terms of Localized Quantities. II. Application to Some Simple Molecules. *J. Chem. Phys.* **1982**, *76*, 1919–1933.

(47) Schindler, M.; Kutzelnigg, W. Theory of Magnetic Susceptibilities and NMR Chemical Shifts in Terms of Localized Quantities. 3. Application to Hydrocarbons and Other Organic Molecules. *J. Am. Chem. Soc.* **1983**, *105*, 1360–1370.

(48) London, F. Théorie Quantique Des Courants Interatomiques Dans Les Combinaisons Aromatiques. *J. Phys. Radium* **1937**, *8*, 397–409.

(49) Ditchfield, R. Molecular Orbital Theory of Magnetic Shielding and Magnetic Susceptibility. *J. Chem. Phys.* **1972**, *56*, 5688–5691.

(50) Tellgren, E. I.; Soncini, A.; Helgaker, T. Nonperturbative ab initio Calculations in Strong Magnetic Fields Using London Orbitals. *J. Chem. Phys.* **2008**, *129*, 154114.

(51) Irons, T. J.; Zemen, J.; Teale, A. M. Efficient Calculation of Molecular Integrals over London Atomic Orbitals. *J. Chem. Theory Comput.* **2017**, *13*, 3636–3649.

(52) Sen, S.; Tellgren, E. I. Non-Perturbative Calculation of Orbital and Spin Effects in Molecules Subject to Non-Uniform Magnetic Fields. *J. Chem. Phys.* **2018**, *148*, 184112.

(53) Sun, S.; Williams-Young, D.; Stetina, T. F.; Li, X. Generalized Hartree-Fock with Non-perturbative Treatment of Strong Magnetic Field: Application to Molecular Spin Phase Transition. *J. Chem. Theory Comput.* **2019**, *15*, 348–356.

(54) Kutzelnigg, W. Relativistic corrections to magnetic properties. *J. Comput. Chem.* **1999**, *20*, 1199–1219.

(55) Aucar, G. A.; Saue, T.; Visscher, L.; Jensen, H. J. A. On the Origin and Contribution of the Diamagnetic Term in Four-Component Relativistic Calculations of Magnetic Properties. *J. Chem. Phys.* **1999**, *110*, 6208–6218.

(56) Komorovský, S.; Repiský, M.; Malkina, O. L.; Malkin, V. G.; Malkin Ondík, I.; Kaupp, M. A Fully Relativistic Method for Calculation of Nuclear Magnetic Shielding Tensors with a Restricted Magnetically Balanced Basis in the Framework of the Matrix Dirac-Kohn-Sham Equation. *J. Chem. Phys.* **2008**, *128*, 104101.

(57) Sun, Q.; Liu, W.; Xiao, Y.; Cheng, L. Exact Two-Tomponent Relativistic Theory for Nuclear Magnetic Resonance Parameters. *J. Chem. Phys.* **2009**, *131*, 081101.

(58) Autschbach, J. Relativistic Effects on Electron–Nucleus Hyperfine Coupling Studied with an Exact 2-Component (X2C) Hamiltonian. *J. Chem. Theory Comput.* **2017**, *13*, 710–718.

(59) Wodyński, A.; Kaupp, M. Density Functional Calculations of Electron Paramagnetic Resonance g- and Hyperfine-Coupling Tensors Using the Exact Two-Component (X2C) Transformation and Efficient Approximations to the Two-Electron Spin–Orbit Terms. *J. Phys. Chem. A* **2019**, *123*, 5660–5672.

(60) Dyall, K. G. Interfacing Relativistic and Nonrelativistic Methods. I. Normalized Elimination of the Small Component in the Modified Dirac Equation. *J. Chem. Phys.* **1997**, *106*, 9618–9626.

(61) Dyall, K. G. Interfacing Relativistic and Nonrelativistic Methods. II. Investigation of a Low-Order Approximation. *J. Chem. Phys.* **1998**, *109*, 4201–4208.

(62) Dyall, K. G.; Enevoldsen, T. Interfacing Relativistic and Nonrelativistic Methods. III. Atomic 4-Spinor Expansions and Integral Approximations. *J. Chem. Phys.* **1999**, *111*, 10000–10007.

(63) Dyall, K. G. Interfacing Relativistic and Nonrelativistic Methods. IV.. One- and Two-Electron Scalar Approximations. *J. Chem. Phys.* **2001**, *115*, 9136–9143.

(64) Kutzlenigg, W.; Liu, W. Quasirelativistic Theory Equivalent to Fully Relativistic Theory. *J. Chem. Phys.* **2005**, *123*, 241102.

(65) Liu, W.; Peng, D. Infinite-Order Quasirelativistic Density Functional Method Based on the Exact Matrix Quasirelativistic Theory. *J. Chem. Phys.* **2006**, *125*, 044102.

(66) Peng, D.; Liu, W.; Xiao, Y.; Cheng, L. Making Four- and Two-Component Relativistic Density Functional Methods Fully Equivalent Based on the Idea of From Atoms to Molecule. *J. Chem. Phys.* **2007**, *127*, 104106.

(67) Ilias, M.; Saue, T. An Infinite-Order Relativistic Hamiltonian by a Simple One-Step Transformation. *J. Chem. Phys.* **2007**, *126*, 064102.

(68) Liu, W.; Peng, D. Exact Two-component Hamiltonians Revisited. *J. Chem. Phys.* **2009**, *131*, 031104.

(69) Liu, W. Ideas of Relativistic Quantum Chemistry. *Mol. Phys.* **2010**, *108*, 1679–1706.

(70) Li, Z.; Xiao, Y.; Liu, W. On the Spin Separation of Algebraic Two-Component Relativistic Hamiltonians. *J. Chem. Phys.* **2012**, *137*, 154114.

(71) Peng, D.; Middendorf, N.; Weigend, F.; Reiher, M. An Efficient Implementation of Two-Component Relativistic Exact-Decoupling Methods for Large Molecules. *J. Chem. Phys.* **2013**, *138*, 184105.

(72) Egidi, F.; Goings, J. J.; Frisch, M. J.; Li, X. Direct Atomic-Orbital-Based Relativistic Two-Component Linear Response Method for Calculating Excited-State Fine Structures. *J. Chem. Theory Comput.* **2016**, *12*, 3711–3718.

(73) Goings, J. J.; Kasper, J. M.; Egidi, F.; Sun, S.; Li, X. Real Time Propagation of the Exact Two Component Time-Dependent Density Functional Theory. *J. Chem. Phys.* **2016**, *145*, 104107.

(74) Konecny, L.; Kadek, M.; Komorovsky, S.; Malkina, O. L.; Ruud, K.; Repisky, M. Acceleration of Relativistic Electron Dynamics by Means of X2C Transformation: Application to the Calculation of Nonlinear Optical Properties. *J. Chem. Theory Comput.* **2016**, *12*, 5823–5833.

(75) Egidi, F.; Sun, S.; Goings, J. J.; Scalmani, G.; Frisch, M. J.; Li, X. Two-Component Non-Collinear Time-Dependent Spin Density Functional Theory for Excited State Calculations. *J. Chem. Theory Comput.* **2017**, *13*, 2591–2603.

(76) Liu, J.; Cheng, L. Relativistic Coupled-Cluster and Equation-of-Motion Coupled-Cluster Methods. *WIREs Comput. Mol. Sci.* **2021**, *11*, 1536.

(77) Sharma, P.; Jenkins, A. J.; Scalmani, G.; Frisch, M. J.; Truhlar, D. G.; Gagliardi, L.; Li, X. Exact-Two-Component Multiconfiguration Pair-Density Functional Theory. *J. Chem. Theory Comput.* **2022**, *18*, 2947–2954.

(78) Lu, L.; Hu, H.; Jenkins, A. J.; Li, X. Exact-Two-Component Relativistic Multireference Second-Order Perturbation Theory. *J. Chem. Theory Comput.* **2022**, *18*, 2983–2992.

(79) Hoyer, C. E.; Hu, H.; Lu, L.; Knecht, S.; Li, X. Relativistic Kramers-Unrestricted Exact-Two-Component Density Matrix Renormalization Group. *J. Phys. Chem. A* **2022**, *126*, 5011–5020.

(80) Hu, H.; Jenkins, A. J.; Liu, H.; Kasper, J. M.; Frisch, M. J.; Li, X. Relativistic Two-Component Multireference Configuration Interaction Method with Tunable Correlation Space. *J. Chem. Theory Comput.* **2020**, *16*, 2975–2984.

(81) Ehrman, J.; Martinez-Baez, E.; Jenkins, A. J.; Li, X. Improving One-Electron Exact-Two-Component Relativistic Methods with the Dirac–Coulomb–Breit-Parameterized Effective Spin–Orbit Coupling. *J. Chem. Theory Comput.* **2023**, *19*, 5785–5790.

(82) Becke, A. D. Density-functional thermochemistry. III. The role of exact exchange. *J. Chem. Phys.* **1993**, *98*, 5648–5652.

(83) Lee, C.; Yang, W.; Parr, R. G. Development of the Colle-Salvetti Correlation-Energy Formula Into a Functional of the Electron Density. *Phys. Rev. B* **1988**, *37*, 785.

(84) Miehlich, B.; Savin, A.; Stoll, H.; Preuss, H. Results Obtained With the Correlation Energy Density Functionals of Becke and Lee Yang and Parr. *Chem. Phys. Lett.* **1989**, *157*, 200–206.

(85) Stephens, P. J.; Devlin, F. J.; Chabalowski, C. F.; Frisch, M. J. Ab Initio Calculation of Vibrational Absorption and Circular Dichroism Spectra Using Density Functional Force Fields. *J. Phys. Chem.* **1994**, *98*, 11623–11627.

(86) Hariharan, P. C.; Pople, J. A. The Influence of Polarization Functions on Molecular Orbital Hydrogenation Energies. *Theor. Chem. Acc.* **1973**, *28*, 213–222.

(87) Francl, M. M.; Pietro, W. J.; Hehre, W. J.; Binkley, J. S.; Gordon, M. S.; DeFrees, D. J.; Pople, J. A. Self-Consistent Molecular Orbital Methods. XXIII. A Polarization-Type Basis Set for Second-Row Elements. *J. Chem. Phys.* **1982**, *77*, 3654–3665.

(88) Frisch, M. J.; Trucks, G. W.; Schlegel, H. B.; Scuseria, G. E.; Robb, M. A.; Cheese-

man, J. R.; Scalmani, G.; Barone, V.; Petersson, G. A.; Nakatsuji, H. et al. Gaussian 16 Revision A.03. Gaussian Inc. Wallingford CT 2016.

(89) Pollak, P.; Weigend, F. Segmented Contracted Error-Consistent Basis Sets of Double- and Triple-ζ Valence Quality for One- and Two-Component Relativistic All-Electron Calculations. *J. Chem. Theory Comput.* **2017**, *13*, 3696–3705.

(90) Noro, T.; Sekiya, M.; Koga, T. Segmented Contracted Basis Sets for Atoms H Through Xe: Sapporo-(DK)-nZP Sets (n=D,T,Q). *Theor. Chem. Acc.* **2012**, *131*, 1–8.

(91) Williams-Young, D. B.; Petrone, A.; Sun, S.; Stetina, T. F.; Lestrange, P.; Hoyer, C. E.; Nascimento, D. R.; Koulias, L.; Wildman, A.; Kasper, J. et al. The Chronus Quantum (ChronusQ) Software Package. *WIREs Comput. Mol. Sci.* **2020**, *10*, e1436.

(92) Li, X.; Williams-Young, D.; Valeev, E. F.; Petrone, A.; Sun, S.; Stetina, T.; Kasper, J. Chronus Quantum, Beta 2 Version. 2018; http://www.chronusquantum.org.

(93) Barth, G.; Bunnenberg, E.; Djerassi, C.; Elder, D.; Records, R. Magnetic circular dichroism studies. Part 10. – Investigations of some carbonyl compounds. *Symp. Faraday Soc.* **1969**, *3*, 49–60.

(94) Kaito, A.; Hatano, M.; Tajiri, A. CNDO Treatment for Faraday B Terms of Some Azaheterocycles. *J. Am. Chem. Soc.* **1977**, *99*, 5241–5246.

(95) Castellan, A.; Michl, J. Magnetic Circular Dichroism of Cyclic π-Electron Systems. 4. Aza Analogues of Benzene. *J. Am. Chem. Soc.* **1978**, *100*, 6824–6827.

(96) Borca, C. N.; Cheng, R. H.; Xu, Q. L.; Liou, S. H.; Stadler, S.; Idzerda, Y. U.; Dowben, P. A. Origin of the Magnetic Moments in $La_{0.65}Pb_{0.35}MnO_3$ Epitaxial Thin Films. *J. Appl. Phys.* **2000**, *87*, 5606–5608.

(97) Takeda, Y.; Okane, T.; Ohkochi, T.; Fujimori, S.-I.; Saitoh, Y.; Yamagami, H.; Yabuta, H.; Takabatake, T. Electronic States of Magnetic Refrigerator Materials $Mn_{0.9}Fe_{1.1}P_{0.55}As_{0.45}$ Using Soft X-Ray Magnetic Circular Dichroism. *J. Phys.: Conf. Ser.* **2010**, *200*, 012199.

(98) Kataoka, T.; Yamazaki, Y.; Singh, V. R.; Sakamoto, Y.; Fujimori, A.; Takeda, Y.; Ohkochi, T.; Fujimori, S.-I.; Okane, T.; Saitoh, Y. et al. Ferromagnetism in ZnO Co-Doped With Mn and N Studied by Soft X-Ray Magnetic Circular Dichroism. *Appl. Phys. Lett.* **2011**, *99*, 132508.

(99) Tusche, C.; Meyerheim, H. L.; Kirschner, J. Observation of Depolarized ZnO(0001) Monolayers: Formation of Unreconstructed Planar Sheets. *Phys. Rev. Lett.* **2007**, *99*, 026102.

(100) Visscher, L.; Dyall, K. Dirac-Fock Atomic Electronic Structure Calculations using Different Nuclear Charge Distributions. *At. Data Nucl. Data Tables* **1997**, *67*, 207–224.

TOC Graphic

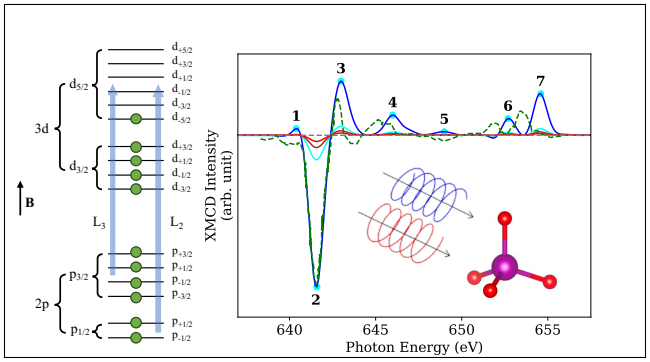
3d
2p
B
L3
L2
XMCD Intensity
(arb. unit)
Photon Energy (eV)
640
645
650
655
1
2
3
4
5
6
7